Single-Phase Charging of Six-Phase Integrated On-Board Battery Charger using Predictive Current Control

Rawan A. Taha, Wessam E. Abdel-Azim, Abdullah Shawier, Mohamed Y. Metwly, Graduate Student Member, *IEEE*, Ayman Samy Abdel-Khalik, Senior Member, *IEEE*, Mostafa S. Hamad, Senior Member, *IEEE*, and Ragi R. Hamdy, Senior Member, *IEEE*, Shady Gadoue, Senior Member, *IEEE*, Shehab Ahmed, Senior Member, *IEEE*

***Abstract*—Integrated On-Board Battery Chargers (IOBCs) have shown promise as an elegant charging solution for electric vehicles in recent literature. Although the three-phase charging technique of IOBCs has extensively been discussed in the literature, single-phase charging is still a challenging research topic. The Predictive Current Control (PCC) approach has shown many benefits, including a straightforward algorithm, simple implementation, comparatively quick response, and appropriate performance, when compared to conventional control techniques. This paper investigates the impact of single-phase charging of a six-phase-based IOBC system with different winding configurations using PCC, which, up to the best authors' knowledge, has not been conceived thus far. Under single-phase charging, the zero-sequence current component is utilized to ensure zero torque production during charging mode. Since the impedance of the zero subspace is highly affected by the employed winding design, the performance of PCC with different winding layouts of either induction machine (IM) or permanent magnet synchronous machine (PMSM) is investigated and compared. The proposed method is experimentally validated using a 1.1kW six-phase IM and a 2 kW 12-slot/10-pole PMSM. Finite Element analysis is also carried out to investigate the effect of single-phase charging mode on the induced radial forces and vibration level when PM machine is employed.**

Rawan A. Taha, Wessam E. Abdel-Azim, Ayman S. Abdel-Khalik and Ragi R. Hamdy are with the Department of Electrical Engineering, Alexandria University, Alexandria, Egypt (email: Rawan.a.taha95@gmail.com, wessam.essam@alexu.edu.eg, ayman. abdel-khalik@alexu.edu.eg and rhamdy @alexu.edu.eg)

A. Shawier is with the School of Electronic Engineering and Computer Science, Queen Mary University, London E14NS, United Kingdom and is also with the Electrical Engineering Department, Faculty of Engineering, Alexandria University, Alexandria 21544, Egypt (e-mail: a.shawier@qmul .ac.uk, abdullah.shawier@alexu.edu.eg)

S. Gadoue are with School of Electronic Engineering and Computer Science, Queen Mary University, London E14NS, United Kingdom (e-mail: s.gadoue@qmul.ac.uk)

Mohamed Y. Metwly is with the Electrical and Computer Engineering Department, University of Kentucky, Lexington 40503, KY, USA, (e-mail: mohamed.metwly@uky.edu).

Mostafa S. Hamad is with the Research and Development Center, Arab Academy for Science, Technology and Maritime Transport, Al Alamein 5060305, Egypt (email: mostafa.hamad@staff.aast.edu)

Shehab Ahmed is with the CEMSE Division at King Abdullah University of Science and Technology, Saudi Arabia (email: shehab.ahmed@kaust .edu.sa)

(Corresponding author: Ayman S. Abdel-Khalik)

***Index Terms*—Asymmetrical six-phase (A6P), dual three-phase (D3P), integrated on-board battery chargers (IOBCs), multiphase machines, predictive current control (PCC), symmetrical six-phase (S6P).**

I. INTRODUCTION

DUE to fossil fuel consumption and CO2 emissions, the dependence on electric vehicles (EVs) has been increasing worldwide at a faster rate [1]. Nevertheless, the charging time and availability of charging outlets comprise the key constraints that affect the expansion of electrically driven vehicles [2]. Many governments have adopted legislative measures to substitute existing internal combustion engine (ICE) vehicles with EVs [3]. According to [4, 5], the market share for electric vehicles has been steadily increasing in the past few decades and is predicted to reach 30% by 2030. However, battery technology has mostly been responsible for the market's expansion. Commercialization of EVs is dependent on the EV battery's weight, price, charging time, and lifetime [6].

Off-board, on-board, and integrated on-board battery chargers (IOBC) with unidirectional and bi-directional power flow capability are the three basic categories into which EV battery chargers can be divided. Bi-directional charging assists in injecting power back into the smart grid, preferably during peak-load hours, while unidirectional charging reduces the amount of hardware needed [7-9]. Compared to off-board and on-board chargers, IOBC mitigates the drawbacks of OBCs and does not affect the vehicle's weight. The IOBC employs the existing propulsion components in the charging process where the power converter acts as a bi-directional DC/AC converter, while the motor windings act as a coupling inductor to smooth the grid line currents [10]. The motor type, the number of phases, and the converter type all determine how effective this technique is [11].

Compared to their three-phase counterparts, multi-phase machines unquestionably have more degrees of freedom, superior fault tolerance, lower converter ratings per phase, and better torque density [12]. As a result, a considerable share of the industry was dominated by six-phase machinery. Six-phase-based IOBC is one of the most promising IOBC systems [11]. A three-phase source or a single-phase source can be used to

supply multi-phase IOBCs [11, 13]; nevertheless, the latter may be more frequently available. The literature has covered three-phase charging of multi-phase-based IOBCs in considerable detail [14, 15]. Despite that [16, 17] discussed various charging topologies of multi-phase IOBCs, single-phase charging remains a challenging technique that needs further studies and consequently, the main aim of this paper is to propose single-phase charging of a six-phase-based IOBC system.

In order to accomplish single phase charging using a six-phase machine, the six-phase stator windings of the machine are considered as two three-phase sets, where the single-phase supply is connected between the two isolated neutral points that should be available. The machine zero-sequence current component is utilized in single-phase charging to exchange energy between battery and grid [11]. The grid current quality, therefore, depends on the stator zero sequence impedance. The effect of stator winding designs and arrangements of IM and PMSM on single-phase IOBC performance has not been investigated so far in the available literature.

A previous study has shown that the winding topology of six-phase stators highly affects the equivalent parameters of different subspaces, which may be determinantal in selecting an optimal winding topology for IOBC applications [18, 19]. As a result, when connecting an IOBC to a single-phase grid, the zero-sequence equivalent reactance is a crucial component that must be taken into account because the higher the machine equivalent reactance is, the smoother the grid current will be [13]. In [17], a split-phase dual inverter PM motor has been proposed for both three-phase and single-phase charging. Under single-phase charging, it has been concluded that the winding leakage inductance is not sufficient to smooth the current waveform and an external line filter is required.

A challenging concern that is also associated with single-phase battery charging is the second-order ripple voltage harmonic on the dc-link voltage due to pulsating power component at twice the line frequency. In the available literature, this problem is minimized either by passive or active filters [20]. In the former, LC resonant circuits are connected across the dc bus to suppress the double line frequency harmonic component. Active filters have also been proposed by connecting them either across the dc-link or the ac sides. Recent proposals have suggested employing some of the stator phases to act as a storage element for active filtering purposes, while the remaining phases are used for line current ripple filtration. In [20], a split-phase double-layer winding has been proposed to achieve this goal.

In recent literature, several control techniques have been introduced to control IOBC systems under three-phase charging [21, 22]. Comparing Predictive Current Control (PCC) to other common control approaches, such as PI controller, where PI parameters tuning might be a bit challenging due to the increased number of sequence current components, PCC has proven to be an effective and simpler control method [23]. By minimizing a cost function, which presents the difference between the reference and measured values, the PCC supplies the inverter with the ideal switching states that minimize this error. The PCC technique for three-phase charging of IOBC has been previously investigated, which makes use of the non-fundamental *xy* subspace in the charging process [24, 25]. On the other hand, single-phase charging control through zero-sequence current component for several multiphase machines with different phase orders has been proposed in [11] using a resonant vector proportional-integral (VPI) controller. However, the PCC approach for single-phase charging has not been addressed thus far.

The main objective of this paper is to investigate the performance of the PCC-based controller under single-phase integrated charging process of EVs of either six-phase IMs or PM machines with possible winding configurations, namely, dual three-phase (D3P), asymmetrical six-phase (A6P) and symmetrical six-phase (S6P) winding configurations. A preliminary case study of this work has been introduced in [26] using a 1.1 kW, 12-phase IM prototype with a full pitch winding design, which can externally be configured with any possible six-phase configuration. The same prototype has also been employed in this paper with another IM with a chorded winding design having the same dimensions and ratings. Moreover, a 2 kW PM machine with Fractional Slot Concentrated Winding (FSCW) has also been employed. PM machines with FSCW are generally designed using various slot/pole combinations [27]; however, one of the promising slot/pole combinations in the literature is the 12/10 combination. For this specific design, only D3P and A6P configurations are possible [16]. Needless to say, D3P and S6P layouts are pretty similar, only the phases order is renumbered. Unlike the work presented in the literature and the preliminary study introduced in [26], the main contributions are summarized as follows:

- The application of the PCC method to a single-phase integrated charger of EVs.
- Possible six-phase winding connections/designs for either IM and PM motor types are compared under integrated single-phase charging of EVs, and their effect on the current quality based on the winding zero sequence inductance is investigated.
- Effect of single-phase charging of PM-based IOBC on the induced radial forces is simulated.
- Experimental results have been conducted to verify theoretical findings.

Accordingly, this paper is divided into multiple sections as follows: Section II illustrates the single-phase charging concept of IOBC as well as the system overview with detailed winding configurations. The PCC is thoroughly described in Section III and used to examine the behavior of the implemented system. The experimental validation is presented in Section IV to investigate and deduce the optimum configuration regarding THD and radial forces effect, which is carried out using Finite Element study in section V. Lastly, the main conclusions are discussed in Section VI.

II. Proposed System Overview

This section presents the six-phase integrated battery charger configuration, highlighting main IOBC components and operational modes. Moreover, the employed winding layouts in

$$\begin{bmatrix} i_\alpha \\ i_\beta \\ i_x \\ i_y \\ i_{0^+} \\ i_{0^-} \end{bmatrix} = \frac{1}{3}\begin{bmatrix} 1 & \cos\frac{2\pi}{3} & \cos\frac{4\pi}{3} & \cos\delta & \cos(\delta+\frac{2\pi}{3}) & \cos(\delta+\frac{4\pi}{3}) \\ 0 & \sin\frac{2\pi}{3} & \sin\frac{4\pi}{3} & \sin\delta & \sin(\delta+\frac{2\pi}{3}) & \sin(\delta+\frac{4\pi}{3}) \\ 1 & \cos\frac{4\pi}{3} & \cos\frac{2\pi}{3} & -\cos\delta & -\cos(\delta+\frac{2\pi}{3}) & -\cos(\delta+\frac{4\pi}{3}) \\ 0 & \sin\frac{4\pi}{3} & \sin\frac{2\pi}{3} & \sin\delta & \sin(\delta+\frac{2\pi}{3}) & \sin(\delta+\frac{4\pi}{3}) \\ 1 & 1 & 1 & 0 & 0 & 0 \\ 0 & 0 & 0 & 1 & 1 & 1 \end{bmatrix}\begin{bmatrix} i_{a1} \\ i_{b1} \\ i_{c1} \\ i_{a2} \\ i_{b2} \\ i_{c2} \end{bmatrix} \quad (1)$$

this study will be elaborated.

A. Six-Phase Integrated OBC Structure

The schematic of a typical six-phase integrated OBC with the proposed PCC-based control block diagram is shown in Fig. 1. Generally, a six-phase integrated charger consists of a six-phase drivetrain, i.e., the machine and the inverter, tied to the battery pack through a DC-DC converter to maintain the DC link voltage at the desired level [11, 21]. The motor propulsion mode is enabled by exciting the fundamental αβ subspace, while the reference currents of the secondary as well as zero subspaces are set to zero [21]. On the other hand, the three-phase charging mode is activated by exciting the secondary *xy* subspace, while the reference *αβ* current components are set to zero to nullify the machine torque production [25].

On the other hand, single-phase charging is carried out through the zero-sequence current component while the *αβ* and *xy* current components are nullified to ensure zero average torque and minimum torque ripple under charging [11]. This can simply be achieved by ensuring same leg voltages for each three-phase set in Fig. 1; hence, the line current is divided equally among the three phases of each set, which is equivalent to a zero-sequence current flow. The grid charging current is filtered by the effect of the winding leakage inductance, which should be equal to ensure equal current sharing among phases. This can be guaranteed for induction machines and PM machines with surface mounted magnets, where the machine air gap is uniform.

The above discussion can simply be proved as follows. The general vector-space-decomposition (VSD) matrix for a six-phase machine with an arbitrary angular displacement δ between the two three-phase winding sets is given by (1) [18].

Under single-phase charging, the controller should ensure the reference phase currents given by (2) and (3).

$$i_{a1} = i_{b1} = i_{c1} = I_m \sin\omega t \quad (2)$$

$$i_{a2} = i_{b2} = i_{c2} = -I_m \sin\omega t \quad (3)$$

Hence, the grid line current will equal.

$$i_g = 3i_{a1} = 3I_m \sin\omega t. \quad (4)$$

By applying the transformation given by (1) for $\delta \in \{0, \pi/6, \pi/3\}$, the sequence current components are given by (5).

$$i_\alpha = i_\beta = i_x = i_y = 0 \text{ and } i_{0^+} = -i_{0^-} = I_m \sin\omega t \quad (5)$$

The same conclusion is obtained for the three winding configurations, as will be confirmed later in the experimental results section.

The proposed single-phase IOBC charger draws high-quality charging currents based on the employed winding design and offers nullified average torque production with simple hardware reconfiguration to switch between the propulsion and changing modes of operation. Moreover, it controls the charging current by regulating the zero-sequence current component and can efficiently underpin the vehicle-to-grid (V2G) concept to enable bidirectional power flow between EVs and the grid [28]. The detailed description of the proposed controller is given in the next section.

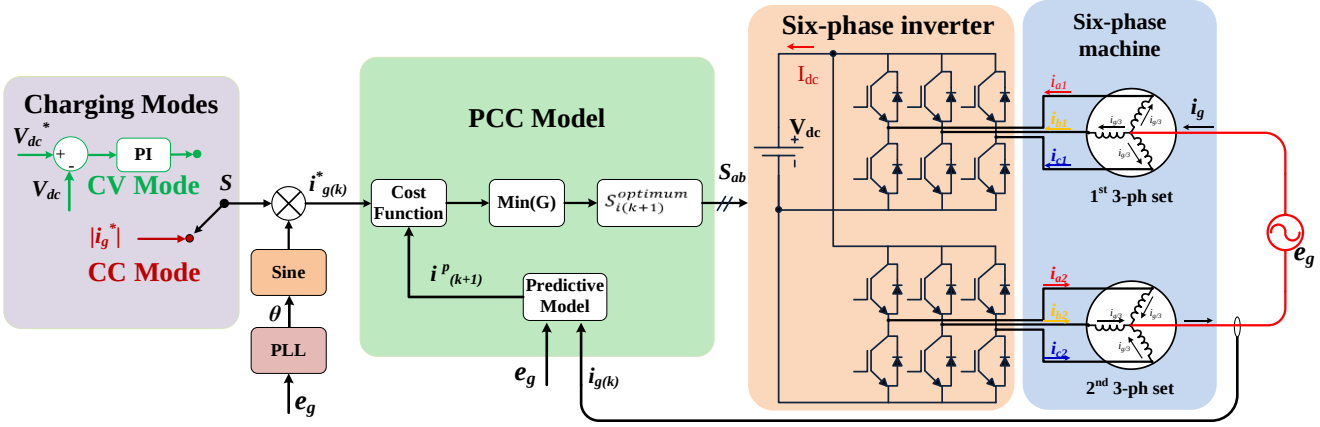

Fig. 1. Proposed Block Diagram of the Single-phase Charger employing a six-phase machine and PCC model.

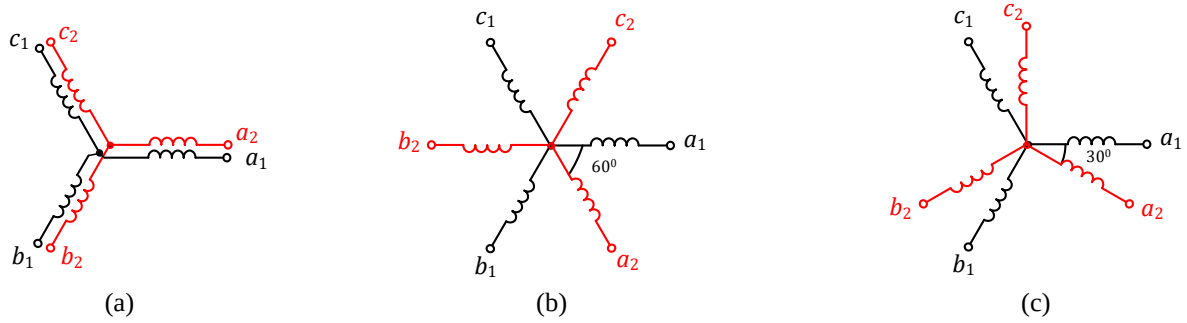

Fig. 2. Different six-phase winding layouts (a) D3P. (b) S6P. (c) A6P.

Phase	A1		A2		B1		B2		C1		C2													
Slot	1	2	3	4	5	6	7	8	9	10	11	12	13	14	15	16	17	18	19	20	21	22	23	24
Upper	A1 +	A2 +	C1 +	C2 +	B1 +	B2 +	A1 +	A2 +	C1 +	C2 +	B1 +	B2 +	A1 +	A2 +	C1 +	C2 +	B1 +	B2 +	A1 +	A2 +	C1 +	C2 +	B1 +	B2 +
Lower	A1 -	A2 -	C1 -	C2 -	B1 -	B2 -	A1 -	A2 -	C1 -	C2 -	B1 -	B2 -	A1 -	A2 -	C1 -	C2 -	B1 -	B2 -	A1 -	A2 -	C1 -	C2 -	B1 -	B2 -

(a)

Phase	A1		A2		B1		B2		C1		C2													
Slot	1	2	3	4	5	6	7	8	9	10	11	12	13	14	15	16	17	18	19	20	21	22	23	24
Upper	A1 +	A2 +	C1 +	C2 +	B1 +	B2 +	A1 +	A2 +	C1 +	C2 +	B1 +	B2 +	A1 +	A2 +	C1 +	C2 +	B1 +	B2 +	A1 +	A2 +	C1 +	C2 +	B1 +	B2 +
Lower	A2 -	C1 -	C2 -	B1 -	B2 -	A1 -	A2 -	C1 -	C2 -	B1 -	B2 -	A1 -	A2 -	C1 -	C2 -	B1 -	B2 -	A1 -	A2 -	C1 -	C2 -	B1 -	B2 -	A1 -

(b)

Phase	A1		A2		B1		B2		C1		C2													
Slot	1		2		3		4		5		6		7		8		9		10		11		12	
	B1 +	B2 +	B2 -	A1 +	A1 -	A2 -	A2 +	C1 -	C1 +	C2 +	C2 -	B1 +	B1 -	B2 -	B2 +	A1 -	A1 +	A2 +	A2 -	C1 +	C1 -	C2 -	C2 +	B1 -

(c)

Fig. 3. A6P winding arrangements. (a) unchorded IM. (b) IM with chorded winding of 5/6 coil span. (c) PM machine with FSCW.

B. Possible Six-Phase Winding Layouts/Configurations

It has been proved in [19] that the winding design can highly affect the equivalent sequence parameters of different six-phase topologies. Under single-phase charging, energy exchange between the grid and battery pack is carried out through the flow of zero sequence current component in the stator winding. Hence, the zero-sequence impedance will highly affect the quality of the stator phase as well as grid line currents. Therefore, this paper investigates the performance of the following six-phase machines; namely, a 24-slot/4-pole unchorded IM, 24-slot/4-pole IM with a chorded winding of 5/6 coil span, and 12-slot/10-pole FSCW-based PM machine. Chorded winding design generally offers better flux distribution, while unchorded winding corresponds to higher non fundamental sequence inductances, and hence, a better current quality is achieved [19].

The possible six-phase winding configurations are D3P ($\delta = 0^{\circ}$), S6P ($\delta = 60^{\circ}$), and A6P ($\delta = 30^{\circ}$) configurations, where δ is the spatial phase shift between the two three-phase winding sets, as shown in Fig. 2. The IMs can accommodate the three possible configurations, while the 12/10 FSCW-based PM machine can only be equipped with D3P and A6P. It is worth mentioning that other slot/pole combinations can be equipped with the three possible winding arrangements, e.g., 24-slot/22-pole and 36-slot/34-pole [29, 30]. The connections of different stator terminals to obtain the three winding arrangements of six-phase IM can be reviewed in [18]. However, the two possible winding arrangements when a 12/10 FSCW PM machine is employed are given in [31]. As an illustrative example, the A6P winding arrangement for the three machines is depicted in Fig. 3.

III. Proposed Predictive Current Control Scheme

Predictive current control is generally advantageous since the concept is straightforward and simple to apply, multivariable systems are easily taken into account, constraints are easily integrated, and multiple objectives can be achieved simultaneously. By minimizing an objective function that represents the difference between the predicted and reference variables for each possible output, PCC employs a mathematical model of the system to forecast the future values of the controlled variables for a defined period [25, 32]. The primary drawback of PCC is that it requires fast hardware to run the optimization problem at each iteration. However, this disadvantage was overcome by the rapid development of digital signal processors capabilities in the past few years.

A finite number of possible switching states are generated for power converters, specifically when discussing single-phase grid connected inverters [24]. Consequently, as illustrated in Fig. 1, in order to forecast the behavior of the controlled variables corresponding to each switching state of the inverter

while including the system constraints into account, the PCC model iteratively executes the system mathematical model.

In this paper, the charging behavior is studied under both constant current and constant voltage control schemes. In the former, the reference current is decided based on the required charging level and directly fed to the PCC model. However, for the constant voltage scheme, an external voltage loop is required to derive the required charging current magnitude using a PI controller.

The main objective of the PCC is to ensure that the grid current is following a certain reference current based on the charging level. The grid current should therefore be three times the phase current, which enables battery charging up to rated machine power. However, the maximum charging power level will be limited by the EV supply equipment (22kW in recent commercial single-phase charging couplers) [33]. To ensure equal current sharing among phases, the leakage inductance of all phases should ideally be equal, which can simply be ensured in case of IM or SPM machine, where the machine air gap is uniform. As a result, the *αβ* and *xy* current components are nullified and the charging process is carried out through the zero-sequence current component only. Consequently, it is enough to formulate the cost function based on the zero-sequence current component of the grid current, which represents a notable advantage of the proposed PCC. The control method is described by the following design steps.

A. Cost Function Definition

The system objective function represents the error between the predicted grid current, which equals three-times the phase current, and the input reference current that needs to be minimized. Assuming that the reference current doesn't change in two consecutive steps where $i^*_{(k)} = i^*_{(k+1)}$, the minimization function can be expressed as follows:

$$G = \left| i^*_{(k)} - i_{(k+1)} \right| \tag{6}$$

where $i^*_{(k)}$ is the reference value of grid current synchronized with the grid using a standard Phase-Locked Loop (PLL), $i_{(k)}$ is the measured grid current. Clearly, the cost function for this specific case will be very simple without any weighting factor needed since the *αβ* and *xy* voltage components of the zero-sequence voltages are already zero.

B. Converter Modelling

A model of the converter and its possible switching states is constructed. The concept of a grid-connected single-phase inverter is utilized for its similarity to the six-phase model, where all legs of the first three-phase VSI is fired by the same signal S_a and the second VSI is fired by S_b, where S_a and S_b are the switching states of the two legs of the equivalent single-phase inverter. In other words, the three legs of each group are fired with the same gating to ensure the flow of zero-sequence currents. Moreover, the resistances and inductances of each three-phase set can be seen as a parallel combination since their starting points are connected virtually based on same terminal voltages, while their end points are electrically connected, as demonstrated in Fig. 4. As a result, the equivalent resistance and inductance, R_{eq} and L_{eq}, will be two-thirds of the winding phase resistance and inductance, R_{ph} and L_{ph}, respectively. Moreover, the switching states (S_a, S_b) of the equivalent single-phase inverter can be deduced as follows:

$$S_a = \begin{cases} 1 & , Q_1 = 1 \,\&\, Q_3 = 0 \\ 0 & , Q_1 = 0 \,\&\, Q_3 = 1 \end{cases} \tag{7}$$

$$S_b = \begin{cases} 1 & , Q_2 = 1 \,\&\, Q_4 = 0 \\ 0 & , Q_2 = 0 \,\&\, Q_4 = 1 \end{cases} \tag{8}$$

The value of the voltage vector (v) is obtained from the following equation:

$$v = \begin{cases} 0 & \text{if } (S_a, S_b) = (0,0) \text{ or } (1,1) \\ +V_{dc} & \text{if } (\mathrm{S_a}, \mathrm{S_b}) = (1,0) \\ -V_{dc} & \text{if } (\mathrm{S_a}, \mathrm{S_b}) = (0,1) \end{cases} \tag{9}$$

where $\mathrm{V_{dc}}$ is the value of DC link voltage.

C. Grid Side Equivalent Circuit Modelling

The grid behavior can be predicted through building a mathematical model of the whole system. The inverter voltage equation can be deduced from the single-phase inverter circuit as follows:

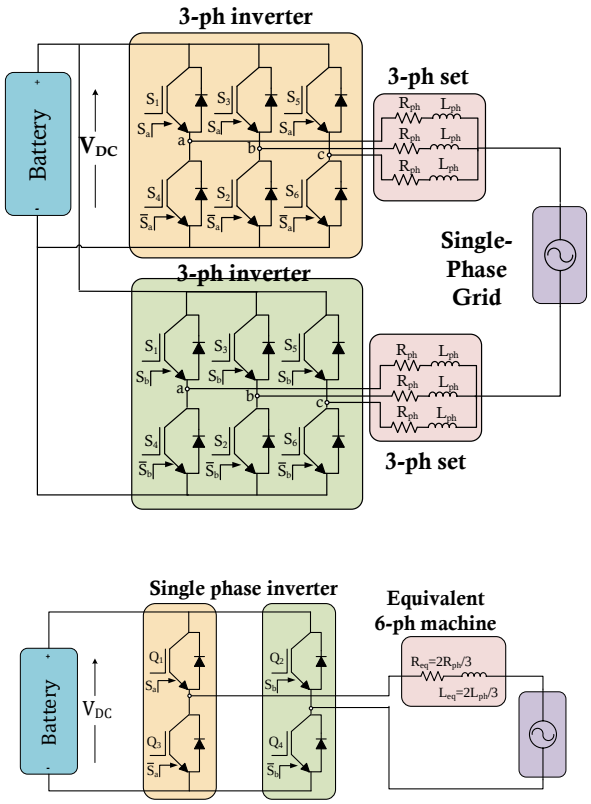

Fig. 4. Proposed inverter scheme (upper figure) Six-phase inverter. (lower figure) Equivalent Single-phase inverter.

$$v = e + L_{eq}\frac{di}{dt} + R_{eq}i \qquad (10)$$

where e is the grid voltage, i is the grid current, and v is the output voltage of the equivalent single-phase inverter.

The grid current is obtained in a discrete time form with sampling time T_s. As a result, the derivative of the grid current can be approximated and expressed as,

$$\frac{di}{dt} \approx \frac{i_{(k+1)} - i_{(k)}}{T_s} \qquad (11)$$

By substituting (6) in (5), an equation of the predicted grid current at step k +1 is deduced:

$$i_{(k+1)} = \left(1 - \frac{R_{eq}T_s}{L_{eq}}\right) i_{(k)} + \frac{T_s}{L_{eq}}(v_{(k)} - e_{(k)}) \qquad (12)$$

where $v_{(k)}$ is the voltage vector corresponding to the four states. To sum up, the measured grid current $i_{(k)}$ and the grid voltage $e_{(k)}$ are used to obtain the predicted grid current and the inverter voltage vector corresponding to each switching state in order to calculate the optimal predicted grid current $i_{(k+1)}$ in the next time interval. The optimal vector that achieves the lowest error between the input reference current and the grid current is then determined using the optimizer.

As a result, the ideal voltage vector and switching state (X) are selected and iterations continue for each time interval. Accordingly, the flowchart presented in Fig. 5 provides an illustration of the PCC control algorithm.

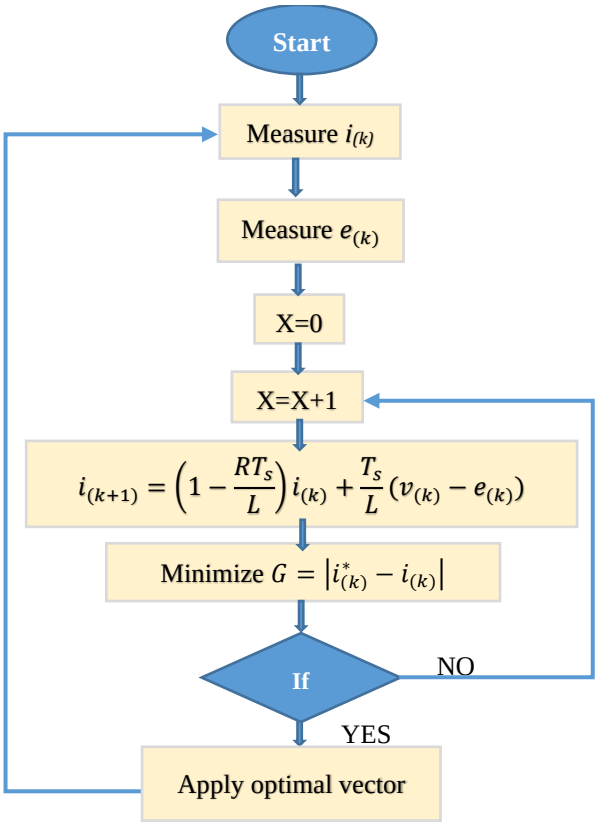

Fig. 5. PCC Algorithm Flowchart.

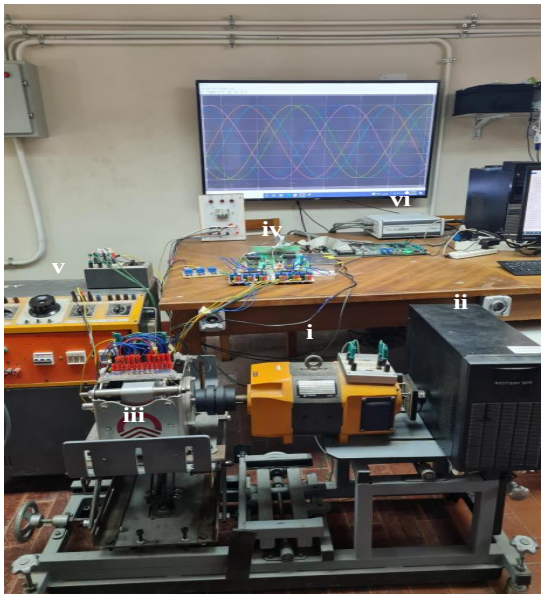

Fig. 6. Test bench: (i) DC machine, (ii) battery box, (iii) six-phase machine, (iv) six-phase inverter, (v) three-phase grid, and (vi) driving controller.

IV. Experimental Validation

A. Experimental Prototype

The theoretical findings presented in this study have been validated using the three prototypes described in section II.B. The prototype machine specifications are listed in Table I. The parameters of each configuration for the chorded/unchorded IMs and the PMSM were obtained using the standard tests given in [18] and are given in Tables II and III, respectively. The single-phase charging process was conducted by controlling each three-phase winding set using a pair of three-phase intelligent power modules (IPMs) (IGCM20F60GA) with a rating of 30A and 600V dc link. A proper heatsink, equipped with a 15V fan, was employed to ensure appropriate cooling for the inverter modules. The IPMs were controlled using a MicroLabBox dSPACE controller version DS1202, with the control-desk environment from dSPACE with a sample time of $T_s = 50\,\mu s$. The analysis and plotting of experimental results were performed using MATLAB software. The current measurements were fed to the dSPACE controller using LA-55P-LEM current transducer with 5 turns, to improve low-current accuracy. Voltage measurements were taken using LV 25-P – LEM. Both current and voltage sensors have a large bandwidth, ranging from 0 Hz to 200 kHz. The overall test bench is shown in Fig. 6.

B. Experimental Results

In this subsection, the proposed PCC-based single-phase charging under both CC and CV modes is implemented. The CC charging was performed at the rated current value of each machine, with a battery pack voltage of 100V for all cases. The behavior of each machine will be presented and discussed separately. Additionally, figures of merit, such as the Total Harmonic Distortion (THD), Average Switching Frequency, and Mean Square Error (MSE), are included to help assess the

performance of each configuration under the proposed single-phase charging-based PCC algorithm. All results are shown per unit based on machine ratings given in Table I. Based on the available battery pack (100 V), the grid voltage is set to 50 V (peak). The reference grid current is set to three times the motor phase current and unity grid power factor is assumed. Based on this initial comparison, the best winding configuration(s) that does not entail an external filter inductance is then recommended. The most promising configuration is then further investigated under CV mode and dynamic conditions.

A. Effect of Winding Configuration on Current Quality

In this subsection, the three available machines are investigated in terms of zero-sequence impedance and their current quality.

TABLE I
PROTOTYPE MACHINE SPECIFICATIONS

Parameter	IM Chorded/Unchorded	PM
Rated Power (kW)	1.1	2
No. of poles	4	10
Rated RMS phase current (A)	2.8	3.2
Rated RMS phase Voltage (V)	110	110
Rated speed (RPM)	1410	1200

TABLE II
PROTOTYPE INDUCTION MACHINES PARAMETERS

Parameter	Chorded IM			Unchorded IM		
	D3P	A6P	S6P	D3P	A6P	S6P
$\boldsymbol{R_s}(\Omega)$	4.18	4.18	4.18	5.00	5.00	5.00
$\boldsymbol{R_r}(\Omega)$	3.46	3.67	3.46	2.90	3.10	2.90
$\boldsymbol{L^s_{\alpha\beta}(mH)}$	9.10	12.0	9.10	10.0	9.60	10.0
$\boldsymbol{L^r_{\alpha\beta}(mH)}$	19.1	16.7	19.1	21.0	22.5	21.0
$\boldsymbol{L^m_{\alpha\beta}(mH)}$	254	247	260	270	304	284
$\boldsymbol{L^s_x(mH)}$	11.8	7.5	11.8	4.44	25.5	4.52
$\boldsymbol{R_{0^+0^-}}(\Omega)$	4.94	4.83	4.89	5.52	5.7	6.08
$\boldsymbol{L^s_{0^+0^-}(mH)}$	5.17	13.97	13.74	7.13	25.71	26.16

TABLE III
PMSM PARAMETERS

Parameter	PM	
	D3P	A6P
$\boldsymbol{R_s}(\Omega)$	1.1	1.1
$\boldsymbol{L^s_{\alpha\beta}(mH)}$	18.3	16.5
$\boldsymbol{R_{0^+0^-}}(\Omega)$	2.12	2.35
$\boldsymbol{L^s_{0^+0^-}(mH)}$	12.82	9.46

1) Chorded IM

The proposed single-phase PCC algorithm was first validated on the six-phase chorded IM with its three possible configurations. Fig. 7 shows the six-phase currents for each configuration. For equal phase resistances, the PCC sees each three-phase set as one of the terminals of the single-phase grid, resulting in identical six-phase currents but opposite direction currents in each three-phase set. Hence, the condition given by (5) is ensured. This can be proved by plotting the sequence current components shown in Fig. 8.

Starting with the D3P configuration, as evident from Fig. 7, the D3P exhibits a highly distorted phase current quality compared to the other two configurations. This can be attributed to the lower inductance of the zero subspace of the D3P, which equals 5.17 mH, as reported in Table II. Conversely, the phase current quality of both A6P and S6P configurations are much better due to their relatively high zero-subspace inductance values of 13.97 mH and 13.74 mH, respectively.

Table IV shows that the THD of phase currents has the highest value of 31.27% for the D3P, while both A6P and S6P have relatively low THD values of 8.62% and 8.24%, respectively. It is expected that the grid currents will exhibit similar profiles to the phase currents. As demonstrated in Fig. 7, the lower plots show the grid current and its corresponding grid voltage, indicating that the PCC algorithm successfully achieves unity power factor for all configurations.

As far as the quality of the charging current is concerned, Table IV shows that the grid current of the D3P configuration has a THD of 31.42%, which is as high as its corresponding phase current. On the other hand, the grid current of both A6P and S6P configurations have THD values of 8.81% and 8.24%, respectively, which are relatively low and consistent with their respective phase currents. Additionally, the Average Switching Frequency of the grid currents of the three configurations was around 2.1 kHz (see Table IV). MSE of currents also has relatively small and consistent values for all configurations, as depicted in Table IV.

It is important to note that the configuration with the lowest zero subspace inductance was expected to have the lowest current quality, as the single-phase charging is accomplished through zero sequence current flow.

2) Unchorded IM

In the same manner, Fig. 9 compares the current waveforms of the three configurations of the unchorded IM. By referring to the zero-subspace inductance of each configuration in Table II, it can be observed that the D3P configuration has the smallest impedance of the zero subspace. As a result, the quality of the phase current waveforms for both the A6P and S6P configurations is superior to that of the D3P, as evidenced by the THD values shown in Table IV of 26.27%, 4.64%, and 4.18% for the D3P, A6P, and S6P configurations, respectively.

From the grid perspective, the proposed PCC was able to effectively achieve a unity power factor for all three configurations, as illustrated in Fig. 9. Additionally, the quality of the grid currents was found to be similar to that of the phase currents, as evidenced by the THD and MSE values presented in Table IV. Specifically, the THD values for the D3P, A6P, and S6P configurations were 26.22%, 4.3%, and 4.65%, respectively, and the corresponding MSE values were 4.13%, 0.14%, and 0.14%. Additionally, the average switching frequency of the grid line currents was found to be relatively high for the D3P configuration with 2.5 kHz, as compared to

the 1.9 kHz for the A6P and S6P configurations.

3) PMSM

Fig. 10 presents the performance of single-phase charging using a PMSM with FSCW. For the employed slots/pole combination, only D3P and A6P configurations are possible [16]. It can be observed that the quality of the phase currents waveforms of both D3P and A6P configurations were found to be superior, as demonstrated by THD values of 8.68% and 9.87%, respectively, as given by Table IV. The current quality of D3P configuration is a bit higher thanks to its slightly higher zero sequence inductance, as clear from Table III. Additionally, the analysis of the grid current, as depicted in Fig. 10, revealed that it exhibited a unity power factor and a quality similar to corresponding phase currents, as demonstrated by the THD and MSE values. The THD values for the D3P and A6P configurations were 7.43% and 9.65%, respectively, and the corresponding MSE values were 0.36% and 0.61%, respectively. Furthermore, the average switching frequency of the grid currents under the PCC algorithm for both configurations was found to be around 2.2 kHz.

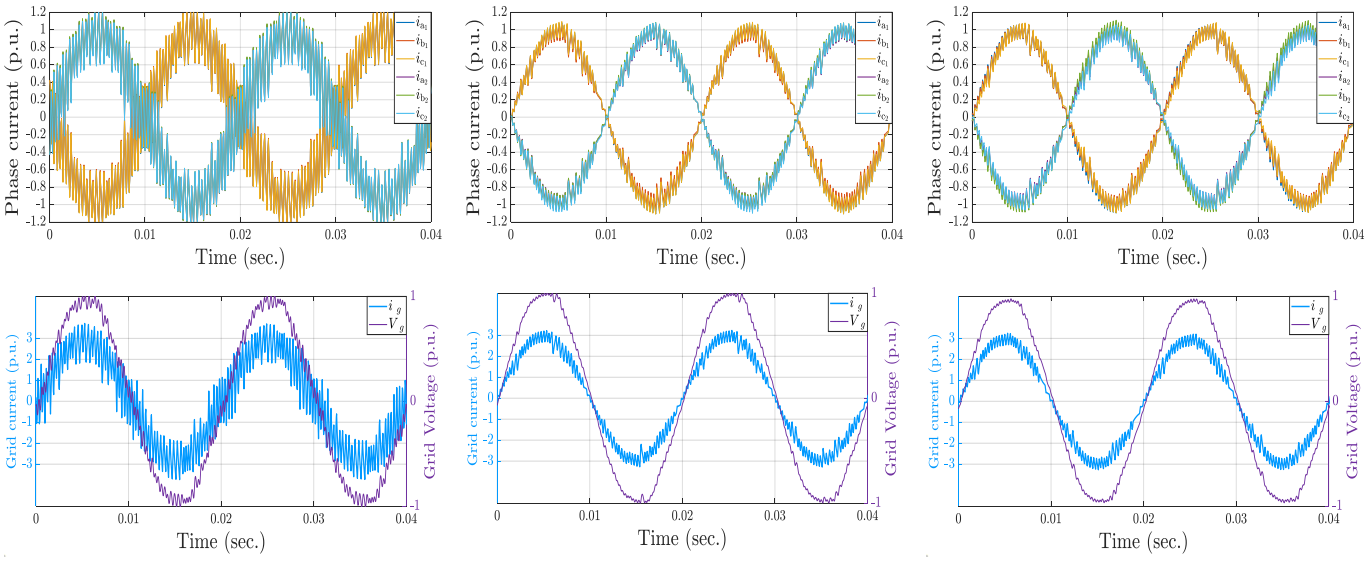

Fig. 7. Six phase currents $i_{a1\rightarrow c2}$ waveforms of chorded IM (upper plots) and the grid line current with their corresponding grid voltage (lower plots) of (a) D3P, (b) A6P, and (c) S6P winding configurations.

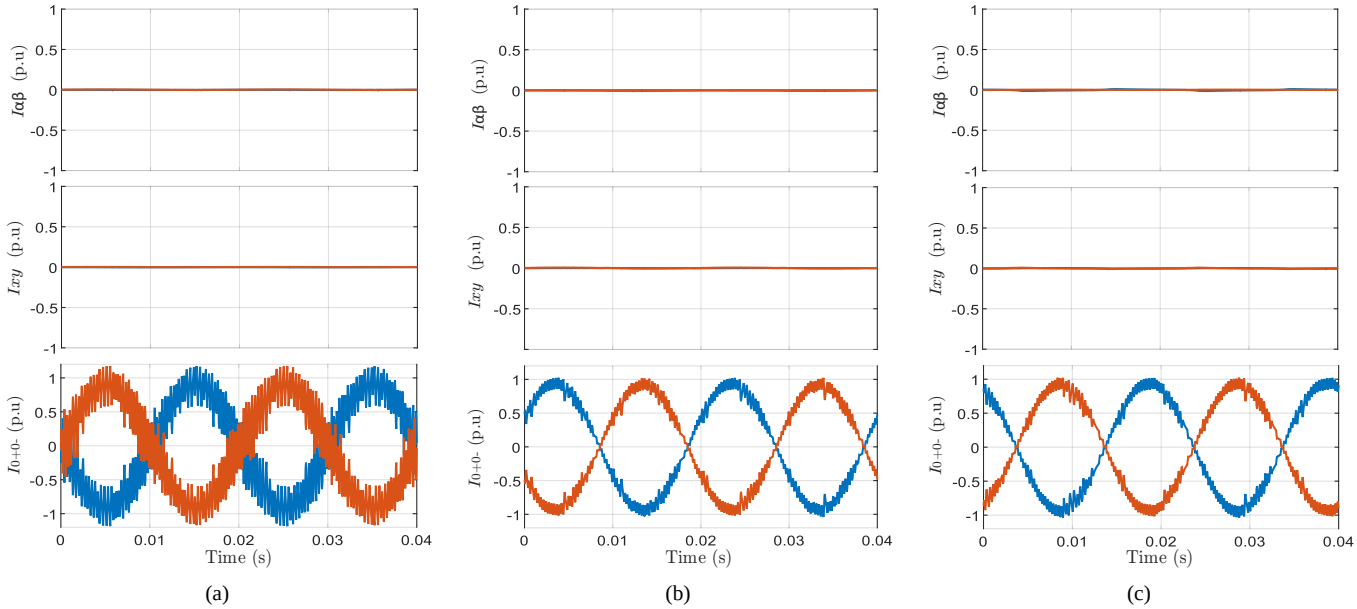

Fig. 8. Sequence currents of the chorded IM with (a) D3P, (b) A6P, and (c) S6P winding configurations.

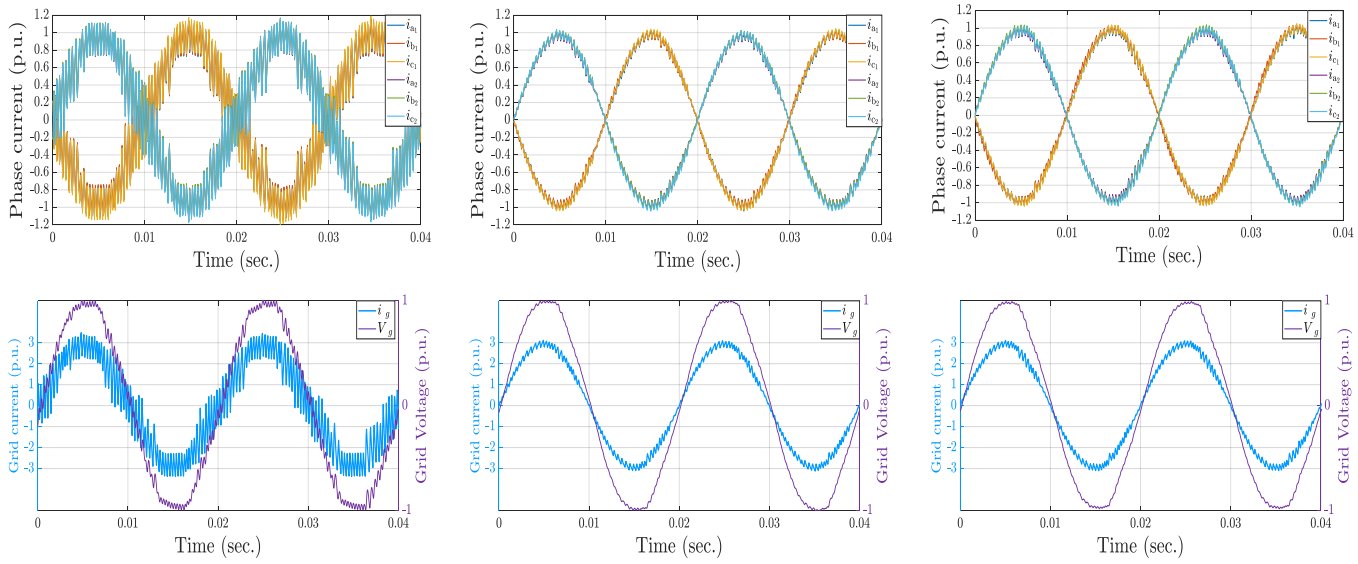

Fig. 9. Six phase currents $i_{a1\rightarrow c2}$ waveforms of unchorded IM (upper plots) and the grid line current with their corresponding grid voltage (lower plots) of (a) D3P, (b) A6P, and (c)S6P winding configurations.

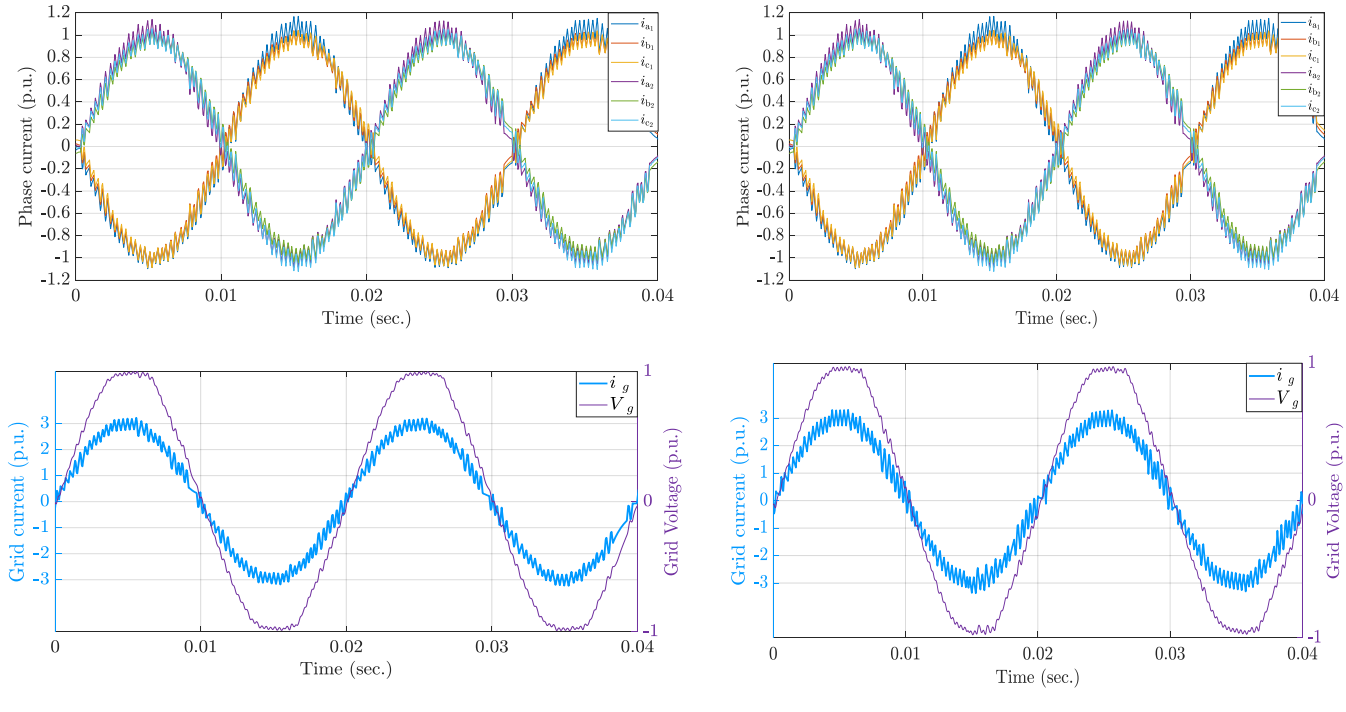

Fig. 10. Six phase currents $i_{a1\rightarrow c2}$ waveforms of PMSM (upper plots) and the grid line current with their corresponding grid voltage (lower plots) of (a) D3P and (b)A6P winding configurations.

B. Dynamic Response of Proposed PCC

In this subsection, the dynamic responses of the proposed PCC under both CC and CV modes are introduced. Based on the comparison given in previous subsection, it seems that both A6P and S6P for induction machine are possible options, where the winding inductance is sufficient to ensure acceptable current quality without an external line inductance. For PMSM machine, both winding layouts are feasible thanks to the relatively large leakage inductance of FSCW in general. Since the machine winding under charging will be equivalent to a simple inductance, it is enough to show the dynamic response using one of the possible options to avoid repetition of results. The A6P induction machine, which is the preferred option under motoring mode, will then be investigated.

1) Constant Current Mode

Under CC mode, the start-up as well as dynamic response of the proposed PCC is investigated by applying a sequence of

step changes of the reference grid current with the following sequence 0, 1, 0, 0.5, 1 p.u. As shown in Fig. 11, the proposed PCC technique was able to rapidly track any step change in the reference current, either from 0 pu to 1 pu or vice versa.

2) Constant Voltage Mode

The proposed controller is then investigated under CV mode, where the reference grid current is derived from the battery voltage error using a PI controller. The PI gains are tuned using trial and error method. It is worth mentioning that under this mode, fast dynamic response is not required since the charging process is already slow. This mode is enabled by switching switch (S) in Fig. 1 from the CC to the CV mode while the reference charging current was initially zero and the battery voltage was less than its base value (100V). The reference battery voltage is set to 106 V (slightly higher than the battery voltage base value of 100 V). Fig. 12 shows the experimental results for this mode, where all variables are given in per unit. Initially, the PI output step increases from zero to the saturation limit of the PI controller (12A), which represents the maximum charging current level, until the error reduces to a certain value. And then, the PI output starts to gradually decrease as the voltage error decreases till the battery voltage reaches its reference value. The same figure shows the filtered battery current, which shows the same response of the RMS grid current.

TABLE IV
FIGURES OF MERITS

Parameter		I_{ph} THD%	I_{grid} THD%	Avg. f_{sw} (kHz)	Computation Time (µs)	MSE of I_{Grids}
Machine	Config.					
Chorded IM	D3P	31.27%	31.42%	2.334	10.4	5.7%
	A6P	8.62%	8.81%	2.113	10.37	0.46%
	S6P	8.2 %	8.24%	2.068	10.4	0.43%
Unchorded IM	D3P	26.27%	26.22%	2.433	10.4	4.13%
	A6P	4.64%	4.3%	1.953	10.37	0.14%
	S6P	4.18%	4.65%	1.906	10.35	0.14%
PM	D3P	8.68%	7.43%	2.208	10.4	0.36%
	A6P	9.87%	9.65%	2.181	10.35	0.61%

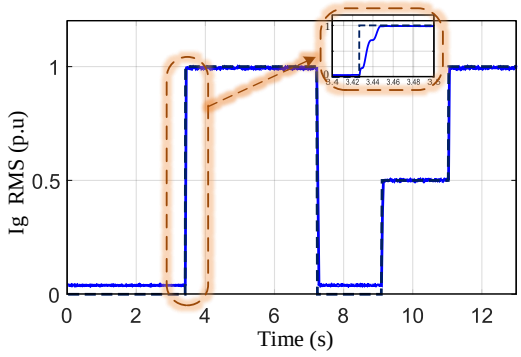

Fig.11. Step response of the charging current in RMS (solid) and its reference (dashed) under CC mode.

V. Finite Element Simulation

To further investigate the effect of single-phase charging on IOBC performance, finite element (FE) simulations have been carried out using the ANSYS Electronics Desktop, shedding light on the torque profiles and radial forces in the charging process. Since the effect of radial forces in IMs with distributed winding is negligible, this section focuses only on the PM machine, where unbalanced magnetic pull may dramatically affect the IOBC performance. Fig. 13 shows the developed torque for the A6P and D3P winding configurations under charging. It is clear that the average torque production is nullified, a basic requirement of the integrated OBCs. Furthermore, the peak-to-peak torque ripple is quite small and can be neglected for both winding configurations. The unbalanced magnetic pull (UMP) is another key issue that affects the performance and lifetime of PM machines. The radial forces exerted on the rotor are computed based on the Maxwell Stress Tensor method [34]. The *x* and *y* components of the UMP are depicted in Fig. 14 for the A6P and D3P layouts in the charging mode, respectively. The comparison shows that the radial forces of the D3P configuration are much higher than the A6P. Thus, the A6P winding layout exhibits better performance than its D3P counterpart; this has also been prior proved in the three-phase charging process [31].

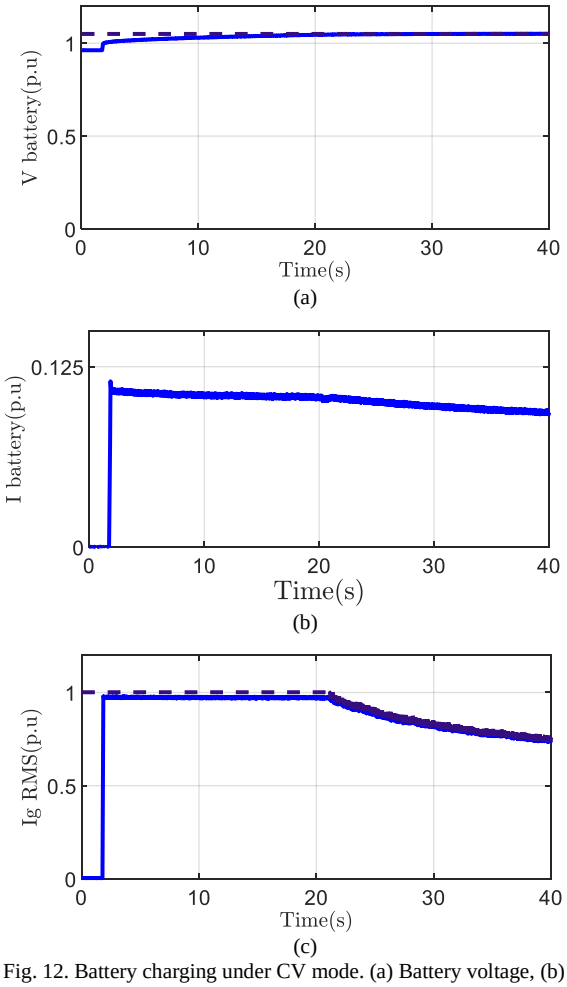

Fig. 12. Battery charging under CV mode. (a) Battery voltage, (b) Battery current and (c) Grid current.

VI. CONCLUSION

In this paper, the Predictive Current Control (PCC) approach was evaluated for the single-phase charging of a six-phase-based integrated on-board battery charger using three different machines with various stator winding configurations. The proposed approach was deduced and validated through experimental results, which demonstrated that the quality of the current is primarily dependent on the equivalent zero-sequence inductance of the employed machine and its stator winding configuration. D3P, A6P and S6P configurations, for chorded and unchorded winding designs, have been studied. For chorded IMs, it was found that the A6P and S6P configurations exhibited superior performance and current quality with lower THD and MSE values of approximately 8% and 0.4%, respectively, while those of the D3P was the worst, at approximately 31% and 5.7%, respectively. A similar conclusion was obtained when evaluating the unchorded IMs. In the case of PMSMs, the grid line currents of the D3P with a THD of 7.43% were found to be of a slightly better quality than those of the A6P configuration, which had a THD of 9.65%. It can be generally concluded that the configuration with a higher zero-subspace inductance results in a higher quality current. Furthermore, the study found that the two types of machines can be electrically regarded as an equivalent series line inductance. However, the mechanical performance differs as the induced radial forces and vibrations during charging have a minor effect on IMs but have a major impact on PMSM with D3P winding, as validated by Finite Element analysis. Finally, although the battery pack can be charged at rated machine power rating, the maximum charging level is limited by the power level of the available commercial charging couplers.

Future work will investigate the possibility to suppress the second order ripple voltage due to the pulsating nature of the input single-phase power as well as operation under fault conditions.

ACKNOWLEDGMENT

This work was achieved by the financial support of ITIDAs ITAC collaborative funded project under the category type of advanced research projects (ARP) and Grant Number ARP2020.R29.7.

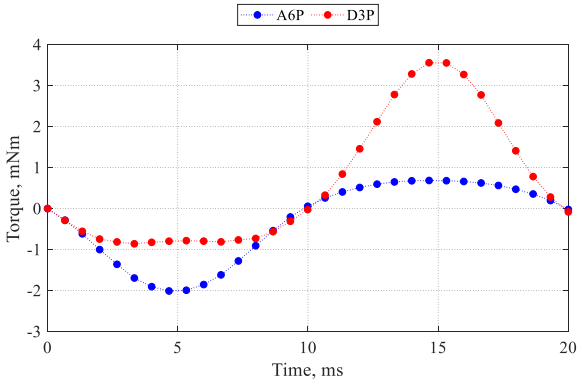

Fig. 13. Torque profiles in the charging mode of operation.

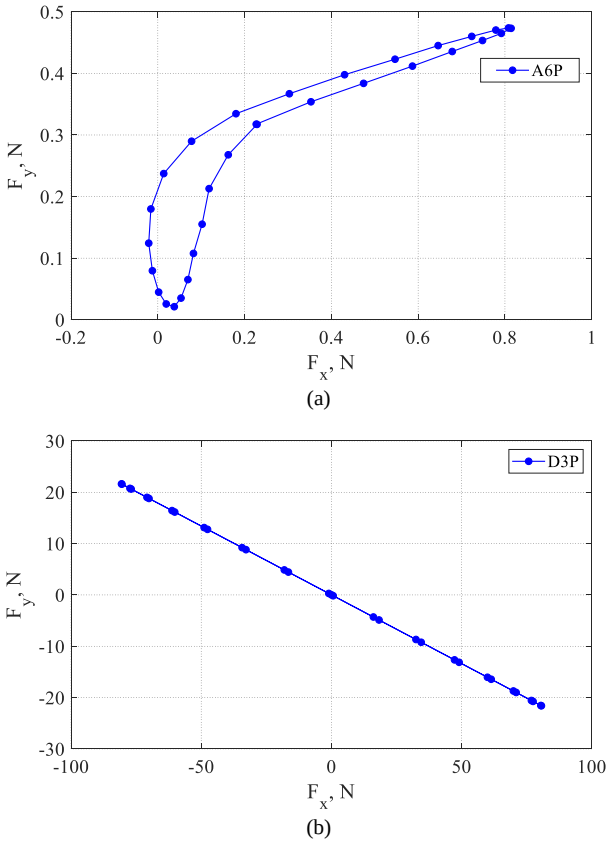

Fig. 14. x-y electromagnetic forces on the rotor in the charging mode. (a) A6P. (b) D3P.

REFERENCES

[1] S. Pazouki, A. Mohsenzadeh, S. Ardalan, and M.-R. Haghifam, "Simultaneous planning of PEV charging stations and DGs considering financial, technical, and environmental effects," *Canadian Journal of Electrical and Computer Engineering*, vol. 38, no. 3, pp. 238-245, 2015.

[2] S. Alshahrani, M. Khalid, and M. Almuhaini, "Electric vehicles beyond energy storage and modern power networks: Challenges and applications," *IEEE Access*, vol. 7, pp. 99031-99064, 2019.

[3] IEA. (2021) Global EV Outlook 2021. Available: https://www.iea.org/reports/global-ev-outlook-2021

[4] E. A. Grunditz and T. Thiringer, "Performance Analysis of Current BEVs Based on a Comprehensive Review of Specifications," *IEEE Transactions on Transportation Electrification*, vol. 2, no. 3, pp. 270-289, 2016, doi: 10.1109/tte.2016.2571783.

[5] N. Kittner, I. Tsiropoulos, D. Tarvydas, O. Schmidt, I. Staffell, and D. M. Kammen, "Electric vehicles," in *Technological Learning in the Transition to a Low-Carbon Energy System*: Elsevier, 2020, pp. 145-163.

[6] E. Roshandel, A. Mahmoudi, S. Kahourzade, A. Tahir, and N. Fernando, "Propulsion System of Electric Vehicles," in *2021 31st Australasian Universities Power Engineering Conference (AUPEC)*, 2021: IEEE, pp. 1-6.

[7] M. Yilmaz and P. T. Krein, "Review of Battery Charger Topologies, Charging Power Levels, and Infrastructure for Plug-In Electric and Hybrid Vehicles," *IEEE Transactions on Power Electronics*, vol. 28, no. 5, pp. 2151-2169, 2013, doi: 10.1109/tpel.2012.2212917.

[8] S. Mahobiya, S. Kumar, and S. K. Gawre, "Investigation of Different Types of Bidirectional Charging Operations of Electric Vehicles," *Recent advances in Power Systems*, pp. 229-243, 2023.

[9] U. Mustafa, R. Ahmed, A. Watson, P. Wheeler, N. Ahmed, and P. Dahele, "A Comprehensive Review of Machine-Integrated Electric Vehicle Chargers," *Energies*, vol. 16, no. 1, p. 129, 2023.

[10] C. Shi, Y. Tang, and A. Khaligh, "A Single-Phase Integrated Onboard Battery Charger Using Propulsion System for Plug-in Electric Vehicles,"

IEEE Transactions on Vehicular Technology, vol. 66, no. 12, pp. 10899-10910, 2017, doi: 10.1109/tvt.2017.2729345.

[11] I. Subotic, N. Bodo, and E. Levi, "Single-Phase On-Board Integrated Battery Chargers for EVs Based on Multiphase Machines," *IEEE Transactions on Power Electronics*, vol. 31, no. 9, pp. 6511-6523, 2016, doi: 10.1109/tpel.2015.2504400.

[12] E. Levi, "Multiphase Electric Machines for Variable-Speed Applications," *IEEE Transactions on Industrial Electronics*, vol. 55, no. 5, pp. 1893-1909, 2008, doi: 10.1109/tie.2008.918488.

[13] S. Haghbin, S. Lundmark, M. Alakula, and O. Carlson, "Grid-Connected Integrated Battery Chargers in Vehicle Applications: Review and New Solution," *IEEE Transactions on Industrial Electronics*, vol. 60, no. 2, pp. 459-473, 2013, doi: 10.1109/tie.2012.2187414.

[14] H. J. Raherimihaja, G. Xu, and Q. Zhang, "Review and Novel Options of Three-Phase Integrated Battery Chargers for EVs," in *2020 IEEE Vehicle Power and Propulsion Conference (VPPC)*: IEEE, pp. 1-5.

[15] M. Tong, M. Cheng, S. Wang, and W. J. I. T. o. I. E. Hua, "An on-board two-stage integrated fast battery charger for EVs based on a five-phase hybrid-excitation flux-switching machine," vol. 68, no. 2, pp. 1780-1790, 2020.

[16] M. Y. Metwly, M. S. Abdel-Majeed, A. S. Abdel-Khalik, R. A. Hamdy, M. S. Hamad, and S. Ahmed, "A Review of Integrated On-Board EV Battery Chargers: Advanced Topologies, Recent Developments and Optimal Selection of FSCW Slot/Pole Combination," *IEEE Access*, vol. 8, pp. 85216-85242, 2020.

[17] S. Haghbin, T. Thiringer, and O. Carlson, "An integrated split-phase dual-inverter permanent magnet motor drive and battery charger for grid-connected electric or hybrid vehicles," in *2012 XXth International Conference on Electrical Machines*, 2012: IEEE, pp. 1941-1947.

[18] A. S. Abdel-Khalik, M. S. Abdel-Majeed, and S. Ahmed, "Effect of winding configuration on six-phase induction machine parameters and performance," *IEEE Access*, vol. 8, pp. 223009-223020, 2020.

[19] M. S. Abdel-Majeed, A. Shawier, A. S. Abdel-Khalik, M. S. Hamad, M. M. Sedky, and N. A. Elmalhy, "General Current Control of Six-Phase-Based Non-Isolated Integrated On-Board Charger with Low Order Harmonic Compensation," *Sustainability*, vol. 14, no. 3, p. 1088, 2022.

[20] Y. Zhang, J. Fang, F. Gao, T. Song, S. Gao, and D. J. Rogers, "Second-harmonic ripple voltage suppression of integrated single-phase pulsewidth modulation rectifier charging system for EVs," *IEEE Transactions on Power Electronics*, vol. 35, no. 4, pp. 3616-3626, 2019.

[21] I. Subotic, V. Katic, N. Bodo, E. Levi, B. Dumnic, and D. Milicevic, "Overview of fast on-board integrated battery chargers for electric vehicles based on multiphase machines and power electronics," *IET Electric Power Applications*, vol. 10, no. 3, pp. 217-229, 2016, doi: 10.1049/iet-epa.2015.0292.

[22] A. K. Seth and M. Singh, "Plant integrated proportional integrating based control design for electric vehicle charger," *Computers and Electrical Engineering*, vol. 105, p. 108522, 2023.

[23] A. Oad, H. G. Ahmad, M. S. H. Talpur, C. Zhao, and A. Pervez, "Green smart grid predictive analysis to integrate sustainable energy of emerging V2G in smart city technologies," *Optik*, vol. 272, p. 170146, 2023.

[24] Y. Xingwu, J. Hongchao, and G. Wei, "Model predictive control of single phase grid-connected inverter," in *2014 IEEE PES Asia-Pacific Power and Energy Engineering Conference (APPEEC)*, 2014: IEEE, pp. 1-4.

[25] A. Habib *et al.*, "Predictive Current Control of Six-Phase IM-Based Nonisolated Integrated On-Board Battery Charger Under Different Winding Configurations," *IEEE Transactions on Power Electronics*, vol. 37, no. 7, pp. 8345-8358, 2022.

[26] R. A. Taha, W. E. Abdel-Azim, A. Shawier, A. S. Abdel-Khalik, M. S. Hamad, and R. R. Hamdy, "Predictive Current Control Based Single Phase Charging of Six-Phase Integrated On-board Battery Charging System," in *2022 23rd International Middle East Power Systems Conference (MEPCON)*, 2022: IEEE, pp. 1-6.

[27] A. M. EL-Refaie, "Fractional-Slot Concentrated-Windings Synchronous Permanent Magnet Machines: Opportunities and Challenges," in IEEE Transactions on Industrial Electronics, vol. 57, no. 1, pp. 107-121, Jan. 2010.

[28] M. Kwon and S. Choi, "An Electrolytic Capacitorless Bidirectional EV Charger for V2G and V2H Applications," *IEEE Transactions on Power Electronics*, vol. 32, no. 9, pp. 6792-6799, 2017, doi: 10.1109/tpel.2016.2630711.

[29] M. A. Frikha, J. Croonen, K. Deepak, Y. Benômar, M. El Baghdadi, and O. Hegazy, "Multiphase Motors and Drive Systems for Electric Vehicle Powertrains: State of the Art Analysis and Future Trends," *Energies*, vol. 16, no. 2, p. 768, 2023.

[30] M. Y. Metwly, A. S. Abdel-Khalik, M. S. Hamad, S. Ahmed, and N. A. Elmalhy, "Multiphase Stator Winding: New Perspectives, Advanced Topologies, and Futuristic Applications," *IEEE Access*, vol. 10, pp. 103241-103263, 2022.

[31] A. Hemeida, M. Y. Metwly, A. S. Abdel-Khalik, and S. Ahmed, "Optimal Design of A 12-Slot/10-Pole Six-Phase SPM Machine with Different Winding Layouts for Integrated On-Board EV Battery Charging," *Energies*, vol. 14, no. 7, p. 1848, 2021.

[32] J. Rodriguez and P. Cortes, *Predictive control of power converters and electrical drives*. John Wiley & Sons, 2012.

[33] S. S. G. Acharige, M. E. Haque, M. T. Arif, N. Hosseinzadeh, K. N. Hasan and A. M. T. Oo, "Review of electric vehicle charging technologies, standards, architectures, and converter configurations," in IEEE Access, vol. 11, pp. 41218-41255, 2023.

[34] K. Meessen, J. Paulides, and E. Lomonova, "Force calculations in 3-D cylindrical structures using Fourier analysis and the Maxwell stress tensor," *IEEE Transactions on Magnetics*, vol. 49, no. 1, pp. 536-545, 2012.

Rawan A. Taha received the B.Sc. degree in electrical engineering from Alexandria University, Alexandria, Egypt, in 2018. She is currently a Teaching Assistant with the Department of Electrical Power, Faculty of Engineering, Egypt-Japan University of Science and Technology. Her current research interests include power electronics, electric vehicles, and control of multiphase drive systems.

WESSAM E. ABDEL-AZIM received the B.Sc. degree in electrical engineering from Alexandria University, Alexandria, Egypt, in 2018. He is currently a Teaching Assistant with the Department of Electrical, Faculty of Engineering, Alexandria University. His current research interests include electric drives, power electronics, and pulsed power applications.

Abdullah Shawier received the B.Sc. and M.Sc. degrees in electrical engineering from Alexandria University, Alexandria, Egypt, in 2016 and 2021. He is currently a lecturer assistant with the Electrical Engineering Department, Faculty of Engineering, Alexandria University, Alexandria, Egypt. His current research interests include electric drives, multiphase machine, model predictive control, battery chargers, and power electronics.

Mohamed Y. Metwly (GS'21) received the B.Sc. degree in electrical engineering from Alexandria University, Alexandria, Egypt, in 2018, and the M.Sc. from the department of Electrical Engineering, Arab Academy for Science, Technology and Maritime Transport (AASTMT), Alexandria, Egypt, in 2022. He is currently a Ph.D. student and research assistant in electrical engineering at the AMPERE Lab, University of Kentucky (UK), USA. His current research interests include machine design, battery chargers, electric vehicles, renewable energy systems, and multi-objective optimization.

Ayman S. Abdel-Khalik (SM'12) received the B.Sc. and M.Sc. degrees in electrical engineering from Alexandria University, Alexandria, Egypt, in 2001 and 2004, respectively, and the Ph.D. degree in electrical engineering from Alexandria University, and Strathclyde University, Glasgow, U.K., in 2009, under a dual channel program. He is currently a Professor with the Electrical Engineering Department, Faculty of Engineering, Alexandria University, Alexandria, Egypt. He serves as an Associate Editor of IEEE Transactions on Industrial Electronics and IET Electric Power Applications Journal. Also, he serves as the Executive Editor of Alexandria Engineering Journal. His current research interests include electrical machine design and modelling, electric drives, energy conversion, and renewable energy.

Mostafa Hamad (SM'19) obtained the B.Sc. and M.Sc. degrees in Electrical Engineering from Alexandria University, Alexandria, Egypt, in 1999 and 2003, respectively, and the Ph.D. degree in Electrical Engineering from Strathclyde University, Glasgow, U.K., in 2009.

Currently he is a Professor in the Department of Electrical and Control Engineering, College of Engineering and Technology, Arab Academy for Science, Technology and Maritime Transport (AASTMT), Alexandria, Egypt. His research interests include power electronics applications in power quality, electric drives, distributed generation, HVDC transmission systems, and renewable energy.

Ragi A. Hamdy (SM'19) received B.Sc. and M.Sc. on 91 and 94 from Alexandria University, Egypt, and Ph.D. on 99 from Heriot-Watt University, UK. He is currently a Professor with the Electrical Engineering Department, Faculty of Engineering, Alexandria University, Alexandria, Egypt. His current research interests include electric machines, Electric Drives, and power electronics.

SHADY GADOUE received the B.Sc. (Hons.) and M.Sc. degrees in electrical and electronic engineering from Alexandria University, Egypt, in 2000 and 2003, respectively, and the Ph.D. degree in power electronics and motor drives control systems from Newcastle University, Newcastle upon Tyne, U.K., in 2009. In 2011, he joined the Electrical Power Research Group, Newcastle University, as a Lecturer. In 2016, he was with the Power and Control Research Group, Imperial College London, as a full time Visiting Research Scholar. In 2017, he joined the School of Engineering and Applied Science, Aston University, Birmingham, U.K., as a Senior Lecturer. He joined the Queen Mary University of London, U.K., in 2021, as an Associate Professor, where he is currently an Associate Professor in electrical and electronic engineering with the School of Electronic Engineering and Computer Science. He has authored and coauthored more than 70 articles in the area of control and identification algorithms of power electronic converters and motor drive systems. He has been listed as one of top 2% world scientists by Stanford University, in October 2020 and October 2021, in energy engineering. His research interests include transport electrification, electric propulsion, energy systems, power electronics and their control systems, and the condition monitoring of batteries and energy storage devices for electric vehicles.

Shehab Ahmed (SM'12) received the B.Sc. degree in electrical engineering from Alexandria University, Alexandria, Egypt, in 1999, and the M.Sc. and Ph.D. degrees from the Department of Electrical and Computer Engineering, Texas A&M University, College Station, TX, USA, in 2000 and 2007, respectively. He was with Schlumberger Technology Corporation, Houston, TX, USA, from 2001 to 2007, developing downhole mechatronic systems for oilfield service products. He was with Texas A&M University at Qatar from 2007 to 2018. He is currently Professor and Program Chiar of the Electrical and Computer Engineering program in the CEMSE Division at King Abdullah University of Science and Technology (KAUST), Saudi Arabia. His research interests include mechatronics, solid-state power conversion, and electric machines.